

Phase-Field Study of the History-Effect of Remelted Microstructures on Nucleation During Additive Manufacturing of Ni-Based Superalloys



MURALI UDDAGIRI, OLEG SHCHYGLO, INGO STEINBACH,
BENJAMIN WAHLMANN, and CAROLIN KOERNER

In the current work we employ multi-phase-field simulations to understand the effect of remelting on microstructure evolution, especially on nucleation of new grains during selective electron beam melting (SEBM) of Ni-based super alloy. The phase-field model is coupled to both mass and heat transport phenomena including release of latent heat of solidification. We run remelting simulations in both as cast and homogenized conditions. Experimental observations show that remelting triggers the nucleation of new grains at the melt pool border. The simulation results shed more light on the local conditions at the melt pool border thereby enhancing our understanding of the mechanisms responsible for the nucleation. The simulation results are validated with experimental results obtained for the Ni–20.5 mol pct Al model binary alloy.

<https://doi.org/10.1007/s11661-023-07004-0>
© The Author(s) 2023

I. INTRODUCTION

IN the era of Industrial Internet of Things (IIoT), manufacturing has become flexible, efficient and precise. This has created the need for smart factories with minimal input and human intervention. In this regard, additive manufacturing (AM) plays a key role in digitalization of industries.^[1,2] As per ASTM standard, AM refers to a class of manufacturing technologies which can be best described as “a process of joining materials to make objects from 3D model data, usually layer upon layer, as opposed to subtractive manufacturing methodologies”.^[3] An overview of various AM processes is given in References 4–7. Due to specific advantages of design flexibility, rapid prototyping, and ability to produce complex geometries, AM is attaining tremendous interest from industry as well as academic research. AM facilitates manufacturing of critical components in aerospace, automobile and bio-medical fields with superior mechanical properties and reduced lead times.^[1,2] Thermal characteristics of AM process include rapid heating and cooling resulting in high thermal gradients and cooling rates. Whereas the chemical characteristics include

non-equilibrium solidification, suppressed phase transformations and finer microstructures. The review article^[8] provides a good overview of various AM technologies currently being employed for manufacturing of Ni-based single crystal (SX) superalloys.

Microstructure plays a key role in determining the mechanical strength of a component. Based on the manufacturing process, we can expect typical microstructures such as equiaxed microstructure in sand casting, columnar microstructure in directional solidification and single crystal microstructure from Bridgman furnace, *etc.* However, with AM it is possible to tailor the microstructure as per the requirement by adjusting the process parameters.^[9] In the manufacturing of single crystal superalloys, one of the key requirements is to suppress the nucleation of stray grains and orient the crystals in one single direction. However, multi-layer build-up in AM results in partial remelting of previously built layers which can act as potential nucleation sites for new grains. Also, repeated heating and cooling cycles facilitate *in situ* heat treatment which results in homogenization of solute segregation left after the solidification. Currently, multiple nucleation mechanisms are reported during solidification under AM conditions. Helmer *et al.*^[10] reported that in SEBM, nucleation of equiaxed grains can be suppressed by carefully selecting scan strategies so that a preferred growth direction is established over many layers. Liu *et al.*^[11] reported that in SLM of AlSi10Mg alloy, high thermal gradients at the melt pool border led to increased nucleation. Different mechanisms have been proposed in other works.^[12–14]

MURALI UDDAGIRI, OLEG SHCHYGLO, and INGO STEINBACH are with the ICAMS, Ruhr Universität Bochum, Universitätsstr.150, 44801, Bochum, Germany. Contact e-mail: murali.uddagiri@rub.de BENJAMIN WAHLMANN and CAROLIN KOERNER are with the Friedrich-Alexander-Universität Erlangen-Nürnberg, Martensstr. 5, 91058 Erlangen, Germany.
Manuscript submitted August 29, 2022; accepted February 7, 2023.

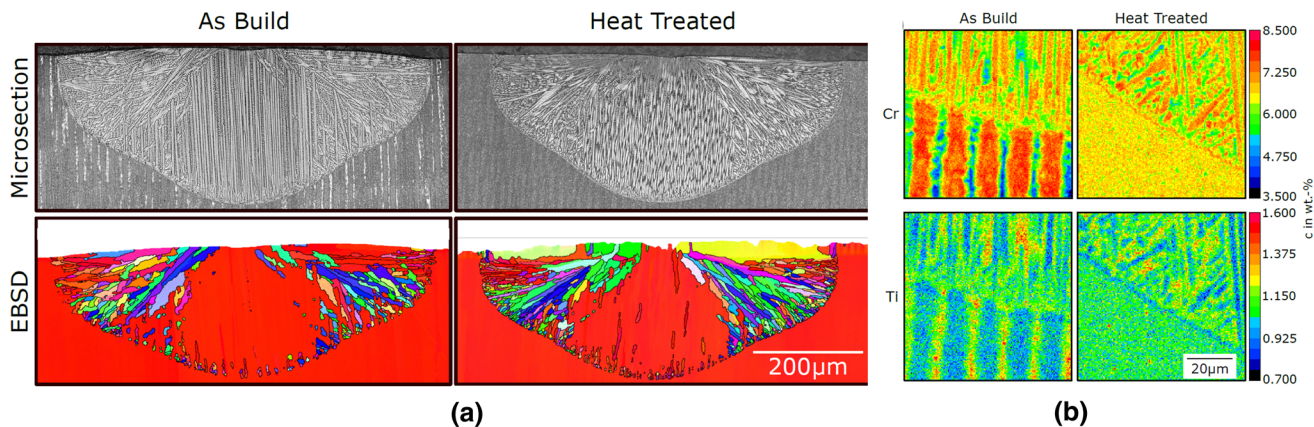


Fig. 1—Experimental results obtained from remelting of as-built and homogenized SX base material. (a) SEM and EBSD images of a single-melt line (300 W and 0.25 m s^{-1}). (b) Concentration distribution of alloying elements Cr and Ti (Reprinted from Ref. [15], under the terms of the Creative Commons CC BY license).

Recently, Rausch *et al.*^[14,15] conducted a more elaborate study to understand the effect of remelting on nucleation mechanism in SEBM of Ni-based SX super alloys in as-built and homogenized condition. In Reference 14 they performed remelting of the IN718 SX material with a wide range of process parameters and observed that the nucleation of new grains predominantly occurs at the melt pool border. In their experiments, it is also observed that out of all the new grains, the grains which are aligned along the thermal gradient direction survived while others are overgrown by epitaxial growth. Based on these observations, they have proposed that nucleation at the melt pool border is triggered by the constitutive undercooling which arises from melting of coarsely segregated interdendritic channels. However, in their extended study of CMSX-4 material,^[16,17] they performed remelting experiment on both as-built and homogenized SX sample.^[15] Based on the experimental results shown in Figure 1, it is observed that under the chosen process conditions nucleation of stray grains is observed at the melt pool border in both as-built and homogenized SX samples. This cannot be explained by their previous ansatz of constitutional undercooling resulting from remelting of interdendritic channels. Hence, we believe that in order to gain deeper understanding of nucleation phenomena, we need to employ microstructure based numerical models.

There exists multiple numerical strategies to understand nucleation and subsequent microstructure evolution in AM,^[18,9] Among them, the phase-field model is the most suitable for understanding nucleation,^[20] competitive grain growth,^[21] CET^[13,22] and solute segregation.^[13,23,24] Due to the flexibility in selecting suitable grid resolutions, phase-field model can accurately resolve the solute diffusion during solidification allowing accurate estimates of solute undercooling which is suspected to be the main driving force for nucleation of new grains.

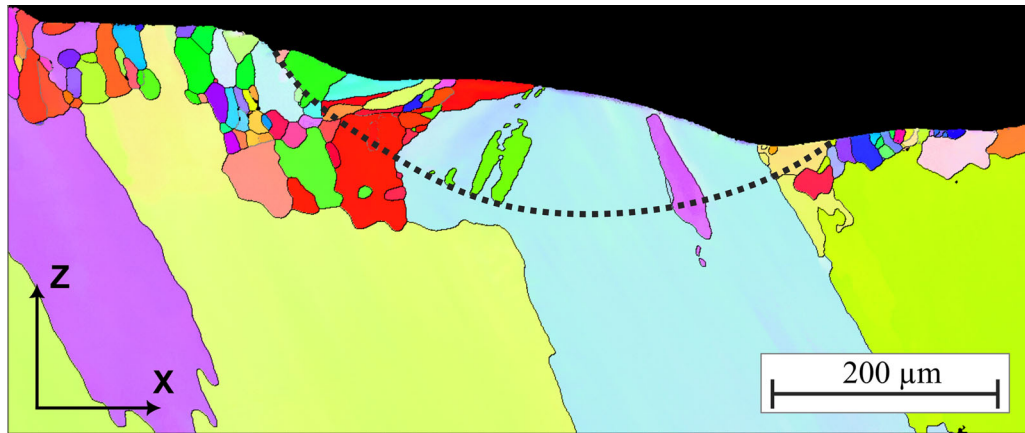
In the current work we employ multi-phase-field (MPF) model coupled to solute and heat diffusion. Instead of applying constant cooling rate and thermal

gradient we impose constant heat extraction rate from the substrate during solidification. Subsequently, remelting is simulated by applying constant positive heat flux at the top surface to mimic the beam melting. As reported in References 25 and 26, in rapid solidification interface heating due to release of latent heat plays a key role in final solidification microstructure and it is only possible to model this phenomena by coupling heat and solute diffusion to the phase-field evolution, which is the main feature of the proposed model. Alternative approaches for modeling of thermal evolution at microstructural scale include solving 1-D thermal diffusion,^[26,27] the freezing temperature approach with constant cooling rate and imposed thermal gradient,^[28] obtaining thermal profile of each layer from coupled macroscopic simulations such as FEM^[23] or CFD.^[29] Schaar *et al.*^[30] in their recent publication presented a similar study for NiAl binary system by imposing constant cooling rate and thermal gradient while for remelting, the system temperature is simply set to a temperature above the liquidus point.

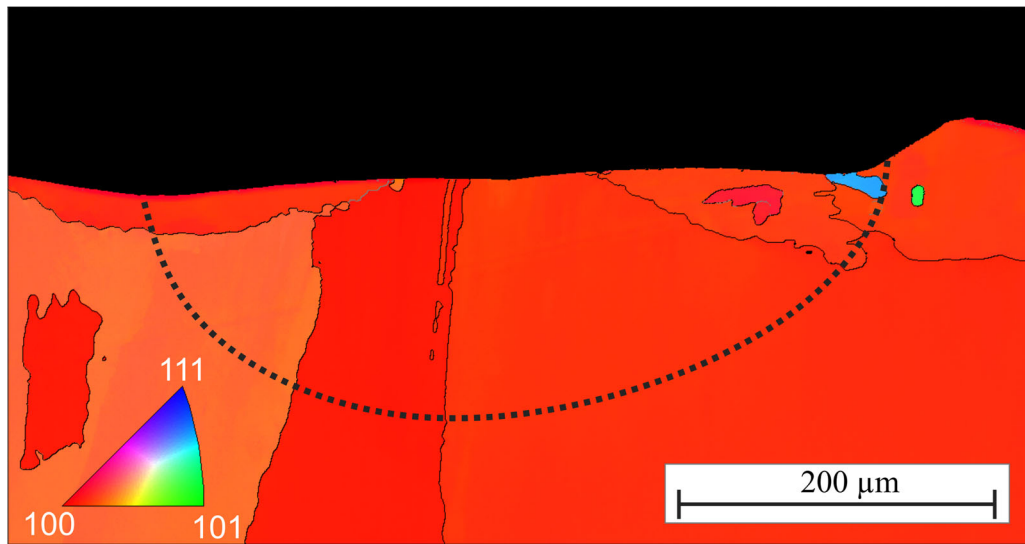
In the current work we limit our study to a Ni–20.5 mol pct Al binary system. Using the phase-field simulations we perform initial solidification, followed by remelting in both as-built and homogenized conditions. Parallely, we also prepared a solid substrate of NiAl binary system of the same composition for experimental study. The details of the experiment are given in Section II.

II. EXPERIMENTS

A sample of Ni–20.5 mol pct Al was produced by vacuum arc melting in a Bühler Arc Melter AM/05 and then machined to a plate of 70 mm × 15 mm × 5 mm (length × width × height). Further processing took place in the ATHENE SEBM system, equipped with an electron gun by pro-beam (AG & Co. KGaA, Gilching, Germany) with an acceleration voltage of 60 kV.^[31] To produce a fine dendritic-cellular microstructure characteristic for alloys fabricated by additive manufacturing,



(a)



(b)

Fig. 2—Grain structure of the melt tracks with (a) 250 W/750 mm s⁻¹ and (b) 300 W/500 mm s⁻¹. The Z direction is the reference direction of the IPF color scale. The melt pool boundaries are delineated by dashed lines (Color figure online).

the surface of the plate was melted with an electron beam with 500 W beam power and 500 mm s⁻¹ scan speed using a snake hatch scan pattern with 200 μm hatch distance. The process chamber was heated to 950 °C to represent the typical processing conditions for Ni-base superalloys as closely as possible.^[32] Afterward, six single lines were melted using two sets of process parameters, three lines for each parameter set: 250 W, 750 mm s⁻¹ and 300 W, 500 mm s⁻¹. Ideally, melting experiments would be done on a single crystal to exclude any effects of grain boundaries on nucleation and dendrite formation. By melting several tracks on a coarse-grained arc-melted sample, the chance of melting over a grain far larger than the width of the track, which can act as a single crystal, is high.

After successful melting and subsequent cooling, the sample was cut and prepared for SEM and EBSD analysis by standard metallurgical procedures with a final polishing using colloidal silica suspension. The microstructure of the melt tracks was analyzed in an FEI Helios NanoLab 600i FIB. The grain structure and orientations were characterized by electron back scatter diffraction (EBSD) using an Oxford Instruments Symmetry S3 EBSD detector. EPMA measurements were performed using a Jeol JXA 8100 to characterize the elemental distribution at the melt pool boundaries. Overview mappings of the melt pools were acquired with a 2.5 μm stepping and mappings of the element distribution at the melt pool boundary with a stepping of 0.25 μm.

EBSD mappings of the grain structure of the single melted tracks are shown in Figure 2. A significantly larger number of grains forms at the melt pool interface in Figure 2(a), though epitaxial solidification prevails

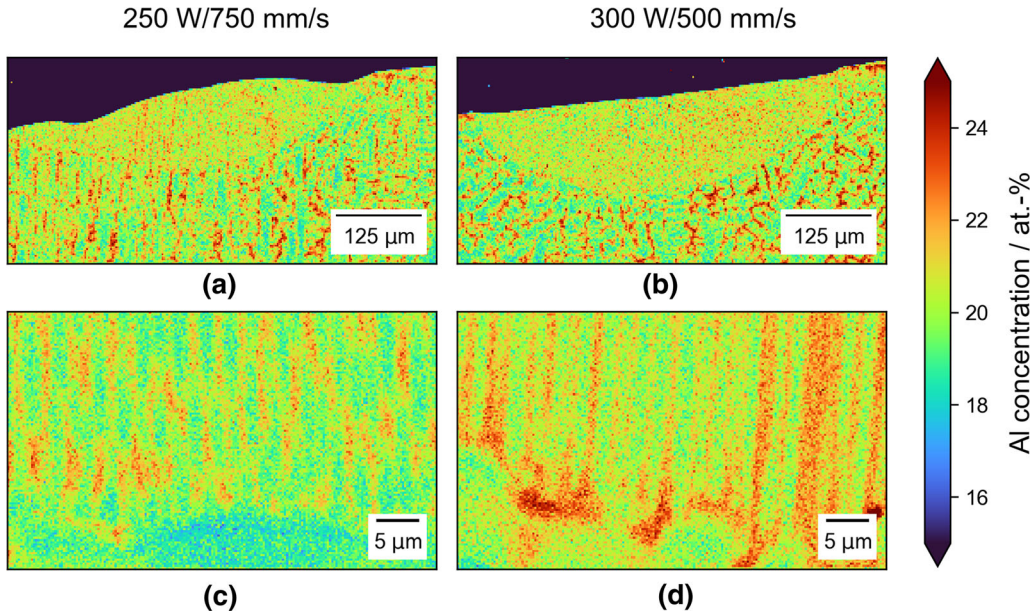


Fig. 3—The concentration of Al for the as-built sample for the two sets of chosen process parameters. (a, b) present the concentration distribution in the whole sample including the deeply remelted zone. (c, d) show concentration distribution at the melt pool border.

for the largest part. Different nucleation behavior is apparent in the left and right halves of the melt pool. Only a single parent grain (colored light blue) extends over the right half of the melt pool interface. This grain is oriented favorably along the heat flow direction, with its 100-direction oriented towards the center of the melt pool. Thereby, epitaxial solidification is facilitated. In contrast, multiple smaller grains are present in the base material along the left half of the melt pool. These are not always oriented along the direction of heat flux. By nucleation, new grains may form whose 100-direction is aligned parallel to the heat flow during cooling.

In contrast to Figure 2(a), the melt track in Figure 2(b) shows nearly perfect epitaxial solidification, as evidenced by the continuation of grain boundaries and orientations across the melt pool interface. Only at the right edge does a single grain nucleate at the melt pool interface. Some new grains also appear in the middle of the melt pool.

Concentration map of Al characterized by EPMA measurements is shown in Figure 3. Figures 3(a) and (b) show the distribution of Al in the whole sample whereas the figures 3(c) and (d) highlight composition distribution at the melt pool boundary for the two sets of parameters 250 W, 750 mm s⁻¹ and 300 W, 500 mm s⁻¹. Since Al has equilibrium partition coefficient of less than one ($k_{eq} < 1$), it tends to segregate into the interdendritic liquid. Hence the composition of Al is high at the interdendritic regions and lower at the core of dendrites. As seen in Figures 3(a) and (b), the segregation of Al is much coarser and predominant in as-built sample compared to the remelted sample.

III. NUMERICAL METHODS

The microstructure evolution is simulated using the MPF model proposed by Steinbach *et al.*^[33–35] One of the biggest advantages of the MPF model is that it considers contributions of all the driving force mechanisms such as thermodynamic, mechanical, convective and electromagnetic which are present during the process. In this work, we restrict our model to free energy contributions of interface energy and chemical energy. Thus, the total free energy of the system is given by

$$F = \int_{\Omega} f_{\text{int}} + f_{\text{ch}}, \quad [1]$$

where f_{int} , and f_{ch} are the interfacial, and chemical free energy densities, respectively. The general form of the interfacial free energy density within the MPF model reads

$$f_{\text{int}} = \sum_{\alpha \neq \beta} \frac{4\sigma_{\alpha\beta}}{\eta} \left[-\frac{\eta^2}{\pi^2} \nabla \phi_{\alpha} \nabla \phi_{\beta} + \phi_{\alpha} \phi_{\beta} \right], \quad [2]$$

and the chemical free energy density has the form

$$f_{\text{ch}} = \sum_{\alpha=1}^N \phi_{\alpha} f_{\alpha}(c_{\alpha}) + \lambda \left[c - \sum_{\alpha=1}^N (\phi_{\alpha} c_{\alpha}) \right], \quad [3]$$

where $\sigma_{\alpha\beta}$ is the interface energy of the phase (or grain) pair α and β and η is the numerical interface width chosen for the simulation convenience.

In Eq. [3], $f_{\alpha}(c_{\alpha})$ is the bulk free energy density of phase α which is a function of the composition of the phase α and λ is the Lagrange multiplier introduced to ensure the mass balance.

Table I. Numerical and Physical Parameters for the Phase-Field Simulations

Data for Ni–20.5 Mol Pct Al		
Equilibrium Slope Between Liquid and γ	m_{01}	– 3.42 K mol pct ⁻¹
Equilibrium Slope Between γ and liquid	m_{10}	–3.76 K mol pct ⁻¹
Equilibrium Slope Between Liquid and γ'	m_{02}	2.87 K mol pct ⁻¹
Equilibrium Slope between γ' and liquid	m_{20}	6.69 K mol pct ⁻¹
Equilibrium Slope Between γ and γ'	m_{12}	77.70 K mol pct ⁻¹
Equilibrium Slope Between γ' and γ	m_{21}	188.58 K mol pct ⁻¹
Diffusivity in Liquid		
Pre-exponential Coefficient	$(D_0)_{\text{liq}}$	1.5e–7 m ² s ⁻¹
Diffusion Activation Energy of Liquid	$(E_A)_{\text{liq}}$	3.7e7 J mol ⁻¹
Diffusivity in γ and γ'		
Pre-exponential Coefficient	$(D_0)_{\text{sol}}$	2.5e–4 m ² s ⁻¹
Diffusion Activation Energy of solid	$(E_A)_{\text{sol}}$	2.5e+5 J mol ⁻¹
Interface Mobility Between Liquid and γ		
Pre-exponential Coefficient	$(M_0)_{01}$	7.5e–7 m ⁴ J ⁻¹ s ⁻¹
Activation Energy	$(E_A)_{01}$	3.7e7 J mol ⁻¹
Interface Mobility Between Liquid and γ^*		
Pre-exponential Coefficient	$(M_0)_{02}$	7.5e–7 m ⁴ J s ⁻¹
Activation Energy	$(E_A)_{02}$	3.7e7 J mol ⁻¹
Interface Mobility Between γ and γ^*		
Pre-exponential Coefficient	$(M_0)_{12}$	1.0e–11 m ⁴ J s ⁻¹
Activation Energy	$(E_A)_{12}$	2.85e4 J mol ⁻¹
Isotropic Interface Stiffness	σ^*	0.24 J m ⁻²
Anisotropy	ϵ	0.35
Latent Heat Liquid to γ	L_{01}	139252.71 J kg ⁻¹
Latent Heat Liquid to γ'	L_{02}	98396.52 J kg ⁻¹
Thermal Conductivity in Liquid	λ_{liq}	50.0 W m K ⁻¹
Thermal Conductivity in γ and γ'	λ_{sol}	75.0 W m K ⁻¹
Heat Capacity of Liquid	$(C_p)_{\text{liq}}$	810.0 J K ⁻¹
Heat Capacity of γ and γ'	$(C_p)_{\text{sol}}$	697.21 J K ⁻¹
Heat Extraction Rate	\dot{q}_{ext}	– 1500 W cm ⁻²
Heat Addition During Remelting	\dot{q}_{beam}	30000 W cm ⁻²
Initial Temperature	T_0	1656 K
Initial Melt Concentration	C_0	20.5 mol pct Al
Grid Spacing	Δx	0.1 μm
Diffuse Interface Width	η	0.45 μm
Numerical Time Increment	Δt	0.1 μs
Box Size Z-Direction	L_z	100 μm
Box Size X-Direction	L_x	50 μm
Box Size Y-Direction	L_y	0 μm

The evolution of phase-field is obtained by the minimization of total free energy:

$$\dot{\phi}_\alpha = - \sum_{\beta}^N \frac{\pi^2 M_{\alpha\beta}}{8\eta N} \left[\frac{\delta F}{\delta \phi_\alpha} - \frac{\delta F}{\delta \phi_\beta} \right], \quad [4]$$

where $M_{\alpha\beta}$ is the interface mobility, F is the total free energy density and N is the number of phase-fields which are present locally. Further, Interface mobility is calculated as a function of temperature in Arrhenius formulation. The activation energies and exponential coefficients for individual phases are given in Table I.

To model the evolution of dendrite microstructure, the phase-field evolution has to be coupled to macroscopic transport phenomena such as thermo-solutal interaction. In the framework of MPF model, the evolution of the total solute composition is modeled by diffusion equation of the form

$$\dot{c} = \nabla \left[\sum_{\alpha} \left(\phi_{\alpha} D^{\alpha} \nabla c_{\alpha} + \sum_{\beta} J_{\alpha\beta} \right) \right], \quad [5]$$

where, D^{α} is the diffusion coefficient in phase α and $J_{\alpha\beta}$ is the anti-trapping current which minimizes the systemic deviation caused by the diffuse interface and variations in solute diffusivity in solid and liquid phases.^[36–38]

As mentioned earlier, heat transfer plays a crucial role in the microstructure development in AM. Most of the existing numerical models which deal with the microstructure evolution in AM still follow constant cooling rate and thermal gradient approximation which is commonly used in directional solidification. However, as explained in Section I, solidification under AM conditions is characterized by strongly varying temperatures and strong fluid flow resulting in rapid solidification. Hence, to accurately model thermal distribution

we couple the phase-field evolution with the heat diffusion equation. The heat diffusion equation is solved implicitly within the time integration loop. This way the temperature at every grid point is calculated based on the local environment and solidification stage. Constant cooling rate is replaced with constant heat extraction rate from the bottom surface and the thermal gradient is established automatically due to strong heat flux from bottom surface. Also, direct coupling between the phase-field and the temperature evolution allows to account for the release of latent heat during solidification.

One more characteristic feature of solidification under AM conditions is the remelting of previously built layers in subsequent layer build-up. To include all possible heat sources, *e.g.* release of latent heat, beam melting and heat extraction from the substrate, we added to the heat diffusion equation the heat source term, \dot{Q}_{local} , which simultaneously handles all the heat sources based on the local environment

$$\rho C_p \dot{T} = \nabla(\lambda \nabla T) + \dot{Q}_{\text{local}}, \quad [6]$$

$$\dot{Q}_{\text{local}} = L \dot{f}_s + \dot{Q}_{\text{substrate}} + \dot{Q}_{\text{beam}}, \quad [7]$$

where ρ is the mass density, C_p is the local heat capacity, $\lambda = \sum_{\alpha} \phi_{\alpha} \lambda_{\alpha}$ is the effective thermal conductivity, L is the solidification latent heat, \dot{f}_s is the local solidification rate, $\dot{Q}_{\text{substrate}}$ is volumetric heat extraction rate through the substrate and \dot{Q}_{beam} is volumetric heat addition due to beam melting.

The volumetric heat sources \dot{Q}_{beam} and $\dot{Q}_{\text{substrate}}$ are assumed to be constant throughout the solidification. They are obtained by dividing the respective heat addition and extraction rates \dot{q}_{beam} and \dot{q}_{ext} with the numerical grid size. Further, to match the thermal boundary conditions with experiments conducted in this work ($P = 300 \text{ W}$, $v = 500 \text{ mm s}^{-1}$), the heat addition rate is calculated from 2D Gaussian heat source model.^[39] Due to the complexities involved with directly measuring the effective cooling rate during AM process, we have adjusted the heat extraction rate to match the cooling rates obtained from macroscopic single line simulations as given in Figure 10 of Reference 14.

In Eq. [6], \dot{Q}_{local} is handled as follows. The evolution of the phase-field parameter ϕ determines the state of solidification and hence the amount of latent heat released. $\dot{Q}_{\text{substrate}}$ is applied on the bottom surface to mimic heat extraction through the substrate. This heat source is kept active during the whole simulation. Similarly, \dot{Q}_{beam} is applied on the top surface to mimic the heat absorption due to beam melting. However, this heat source is only activated for a short period of time based on the simulation requirements. There are multiple criteria to activate and deactivate the heat sources. These include system temperature, *i.e.* minimum and maximum temperature, volume fraction of a given phase, number of time steps or absolute time, *etc.*

Evolution of phase-field along with the solute and heat transport equations are implemented in the open source software package ‘‘OpenPhase’’.^[40,41]

A. Material Input Data

In the current work, numerical simulations are performed for a binary alloy system Ni–20.5 mol pct Al. Phase equilibrium data and corresponding thermodynamic quantities are obtained from Thermo-Calc software.^[42] To facilitate proper thermodynamic description, the binary phase diagram is linearized in the area of interest. Nucleation and growth of liquid phase, primary solid γ phase and eutectic γ' phase are included in the phase-field simulations. Nucleation of both the solid phases is modeled based on the free growth nucleation model proposed by Greer *et al.*^[43] with the following conditions. To mimic the epitaxial growth from the solid substrate, nucleation of primary solid γ phase is allowed only at the bottom surface where the heat extraction is applied. As we are not attempting to nucleate stray grains which nucleate with random orientation, but follow the primary epitaxial grains, the orientation of the primary solid γ phase is fixed and set to grow along Z-axis. However, by studying the local solidification conditions during remelting, we can predict the possibility for nucleation of stray grains. The secondary solid γ' phase is treated as a stoichiometric phase with a fixed composition of 24.0 mol pct Al. It is allowed to nucleate as an eutectic phase towards the end of solidification. The size distribution of the seed particles is defined by a normal distribution function

$$N(d) = K \frac{1}{b\sqrt{2\pi}} \exp - \frac{(d-a)^2}{2b^2}, \quad [8]$$

where K is the user specified nucleation density, d is the diameter of the seed particles, a is the mean seed particles diameter, b is the standard deviation of the normal distribution function. Further details about the nucleation model can be found in References 30 and 44.

Since the temperature window during AM process changes from boiling point of the material to room temperature, to accurately account for the diffusion mechanism, the diffusion coefficients are calculated using the Arrhenius equation. The accuracy of diffusion coefficients is validated against the Thermo-Calc mobility database in the previous study conducted by Schaar *et al.*^[30]

Process parameters and numerical parameters used in the phase-field simulations are given in Table I.

IV. SIMULATION RESULTS AND DISCUSSIONS

A. As-Built Solidification Microstructure

Figure 4 shows the evolution of microstructure and composition distribution of Al at different time steps during the solidification. As discussed in Section III–A, in order to investigate the nucleation phenomena during remelting of the as-built SX sample, we imposed an

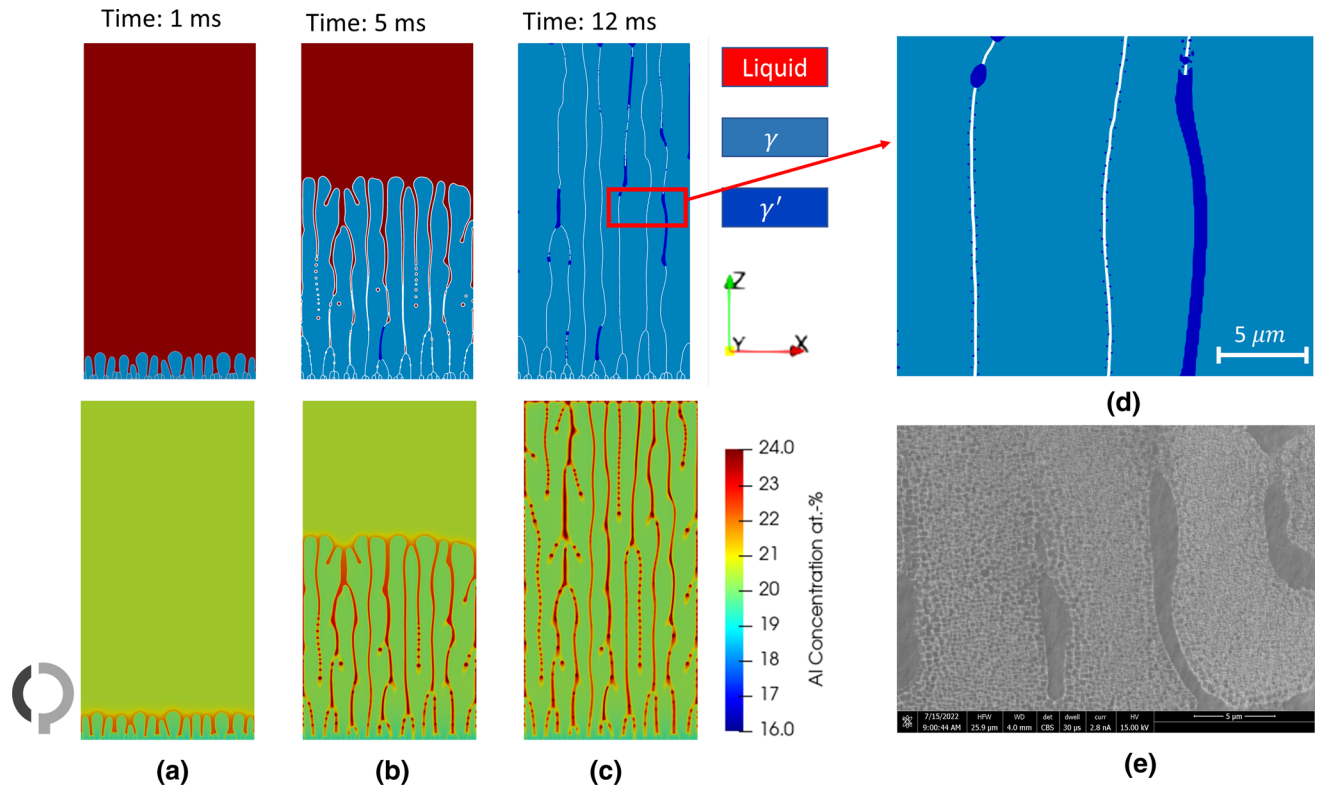


Fig. 4—Evolution of microstructure and corresponding Al composition during initial solidification under AM process conditions at (a) 0.001 s, (b) 0.005 s and (c) 0.012 s of simulated time; (d) is a magnification of the primary γ -particles and (e) is the experimentally observed microstructure highlighting γ' in interdendritic channels.

epitaxial nucleation condition with orientation of new grains set to follow the preferred crystallographic orientation. As the result, the obtained microstructure is not a fully SX microstructure due to the nucleation of multiple dendrites but it allows us to mimic the SX microstructure because all dendrites are oriented in the same preferred direction. This also enables us to study the strong segregation in interdendritic channels at the expense of added grain boundaries. As shown in Figure 4(a), γ phase starts to grow from the bottom wall with grains oriented along the primary growth axis. However, as can be seen in Figure 4(b), due to the established thermal gradient along Z-axis, the dendrite spacing is naturally adjusted according to the imposed heat extraction rate.

As observed in experiments (refer to Figure 3), due to diffusion, Al is segregating into the interdendritic regions. Also, due to the strong thermal gradient, the dendritic spacing is very low compared to that of directional solidification, resulting in the absence of secondary dendrite arms.^[30,32] Thermodynamic calculations conducted using the CALPHAD method show that towards the end of solidification, the secondary γ' phase starts to nucleate at the interdendritic regions, as can be seen at the bottom in Figure 4(b). Figure 4(c) shows the end of solidification, where the liquid phase has been completely transformed into γ and γ' phases. The composition distribution shows that the concentration of Al is highest in the γ' phase and lowest in the trunk regions, where the γ phase is present. The levels of

Al segregation are also in agreement with experimental observations shown in Figures 3(c) and (d).

Magnification of the simulated microstructure (refer to Figure 4(d)) reveals both the morphology and length scale of the microstructure. Owing to the rapid solidification conditions, the primary γ phase grows with cellular morphology with no side arms, and the secondary γ' phase occupies the interdendritic region. The evaluation of the microstructure obtained from the experiments conducted in this work confirms these observations (see Figure 4(e)). Furthermore, the calculated dendrite arm spacing for the imposed thermal boundary conditions is about $5 \mu\text{m}$, which is in good agreement with the experimental observations made for the CMSX-4 alloy under similar processing conditions.^[45,46]

The temperature distribution and the corresponding solidification microstructure are shown in Figure 5. Through the coupled phase-field evolution and heat diffusion, we are able to accurately resolve thermal evolution during solidification. In Figure 5(b), it can be seen that when there is no beam melting, the solid has a strong thermal gradient, while the liquid has a relatively low thermal gradient. The magnified view of solidification front in Figure 5(c) shows that the dendrite tips are the local hot spots due to release of latent heat. The line plots in Figures 5(d) and (e) show the distribution of temperature along Z- and X-axis, respectively. Figure 5(d) illustrates the thermal gradient along the primary growth axis, while Figure 5(e) presents the

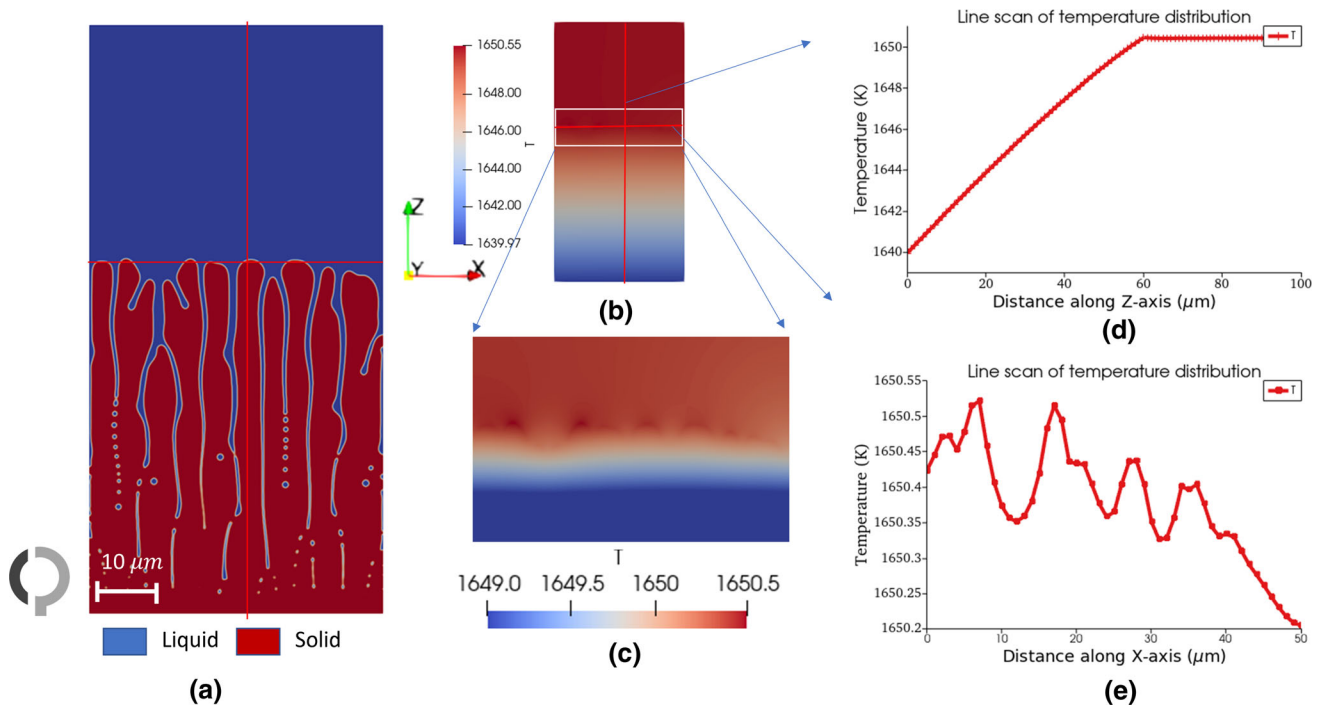


Fig. 5—Evolution of (a) microstructure and (b) temperature during solidification; (c) is the enlarged view of dendrite tips highlighting them as local hot spots due to release of latent heat; (d) is the temperature profile along Z-axis through the center of a dendrite highlighting the effect of latent heat release and showing thermal gradient in solid and liquid phase; (e) is the temperature profile along X-axis across the dendrite tips highlighting non-uniform temperature distribution perpendicular to the direction of heat extraction.

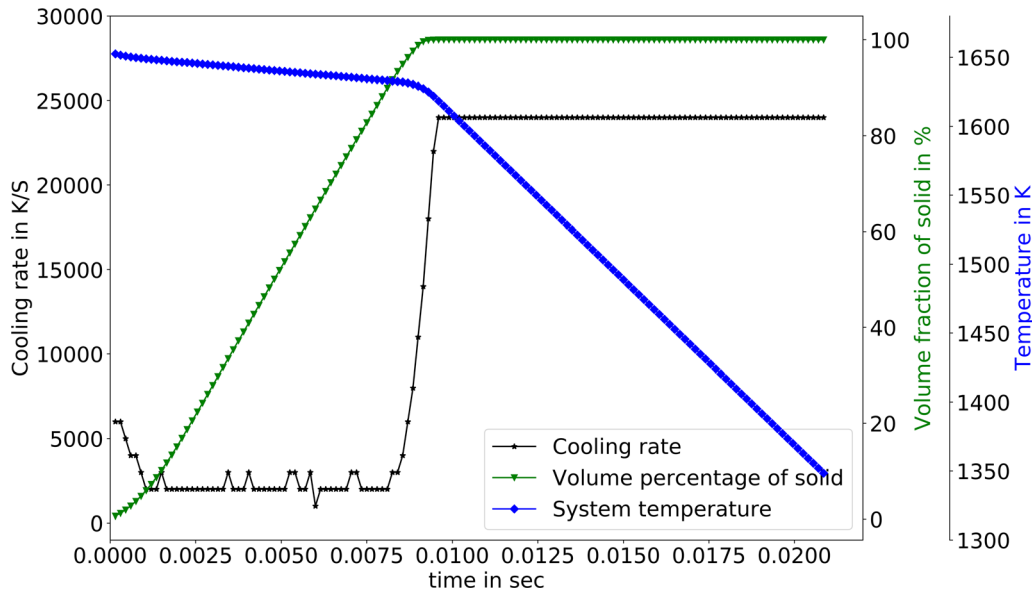


Fig. 6—Evolution of temperature, cooling rate and volume fraction of solid during initial solidification.

non-uniform temperature distribution at the dendrite growth front along X-axis, *i.e.* perpendicular to the primary growth axis. The local variations in the temperature seen in Figure 5(e) are due to the release of latent heat at the dendrite tips. Such hot spots can be resolved only by solving the heat diffusion equation, which treats the release of latent heat as local heat

source. Although solving heat diffusion equation at microstructural length scale involves additional computational effort, it is essential for this study as the main goal is to estimate the constitutional undercooling ahead of the dendrite growth front, which is believed to be responsible for the nucleation of new grains.

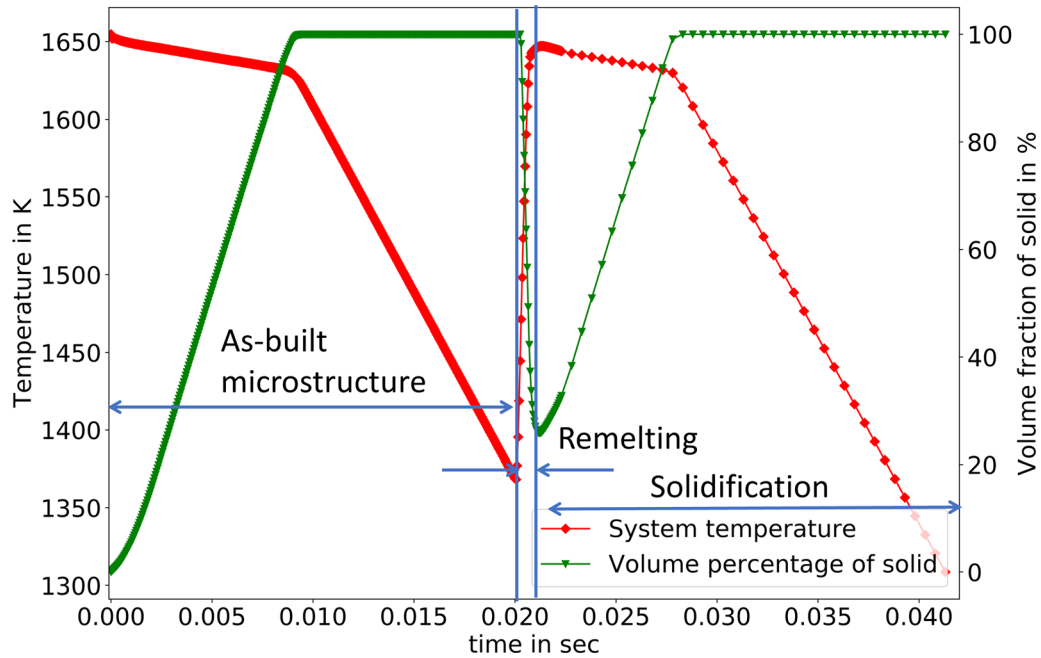


Fig. 7—Evolution of temperature and volume fraction of solid during initial solidification, partial remelting and subsequent solidification.

In Figure 6, the cooling rate, the system average temperature, and the volume fraction of solid are plotted against solidification time. The figure clearly shows that the cooling rate decreases by a factor of more than 10 during solidification due to the release of latent heat. Once the volume fraction of solid reaches 100 pct, the temperature starts to drop with constant cooling rate. From Figure 6 it follows that the end of solidification is reached at around 8 ms. Considering the total height of the system of $100\ \mu\text{m}$, the solidification velocity can be calculated. In our simulations it is $12.5\ \text{mm s}^{-1}$. The calculated solidification velocity is lower than the experimentally observed solidification velocity of $20\ \text{mm s}^{-1}$ ^[32] obtained for CMSX-4 under similar processing conditions. There are many sources for this discrepancy. First, it is the complexity involved in matching the thermal boundary conditions in simulation to the experimental conditions. Second, the measured velocity in PF simulations is *in situ*, *i.e.* velocity observed during the solidification, whereas in the experiments the solidification velocity is estimated at the end of the process. Finally, capturing the solidification velocity experimentally during AM process is extremely difficult due to the rapid solidification.

B. Remelting of As-Built Sample

To study the history-effect in the as-built case, the microstructure obtained in the previous step is remelted and allowed to solidify again. As shown in Figure 7, the initial solidification proceeds until the system temperature reaches 1373 K. At this stage, the heat source at the top, \dot{Q}_{beam} , is activated. Due to the strong heat flux applied at the top, the system temperature quickly rises above the liquidus temperature, initiating melting. The

heat source is kept active until the volume fraction of liquid reaches 60 pct. This is to replicate partial remelting of existing solidification structures during subsequent layer build-up in the AM process.

Figure 8 shows the evolution of microstructure and Al concentration throughout the process of remelting and subsequent solidification. The initial microstructure, shown in Figure 8(a), is obtained from the previous simulation. Due to the applied heat flux, the dendritic microstructure starts to melt from the top, and Al is redistributed in the melt, as shown in Figure 8(b). Figure 8(c) shows the stage where the temperature at the dendrite front drops below the liquidus temperature, resulting in the initiation of epitaxial growth of solid γ phase. However, even at this stage, partial remelting is continued at interdendritic regions due to the presence of γ' phase, which has a lower liquidus temperature due to strong Al segregation. Figure 8(d) shows the later stage of solidification in the remelted zone. As soon as the temperature reaches the γ' solvus temperature, γ' phase starts to re-nucleate, which can be seen at the bottom of the simulation box. As shown in Figure 8(e), at the end of solidification, all the remelted liquid is transformed back into γ and γ' phases.

Figures 9 and 10 present further analysis of the Al distribution and constitutional undercooling at the onset of solidification. Constitutional undercooling is calculated as follows^[47]:

$$\Delta T_c = T_l(C_1^*) - T^* = m_{01}C_1^* + T_m - T^*, \quad [9]$$

where $T_l(C_1^*)$ is the local liquidus temperature, T_m is the melting temperature of pure Ni, m_{01} is the liquidus slope given in Table I, C_1^* and T^* are the composition and temperature of solidification front.

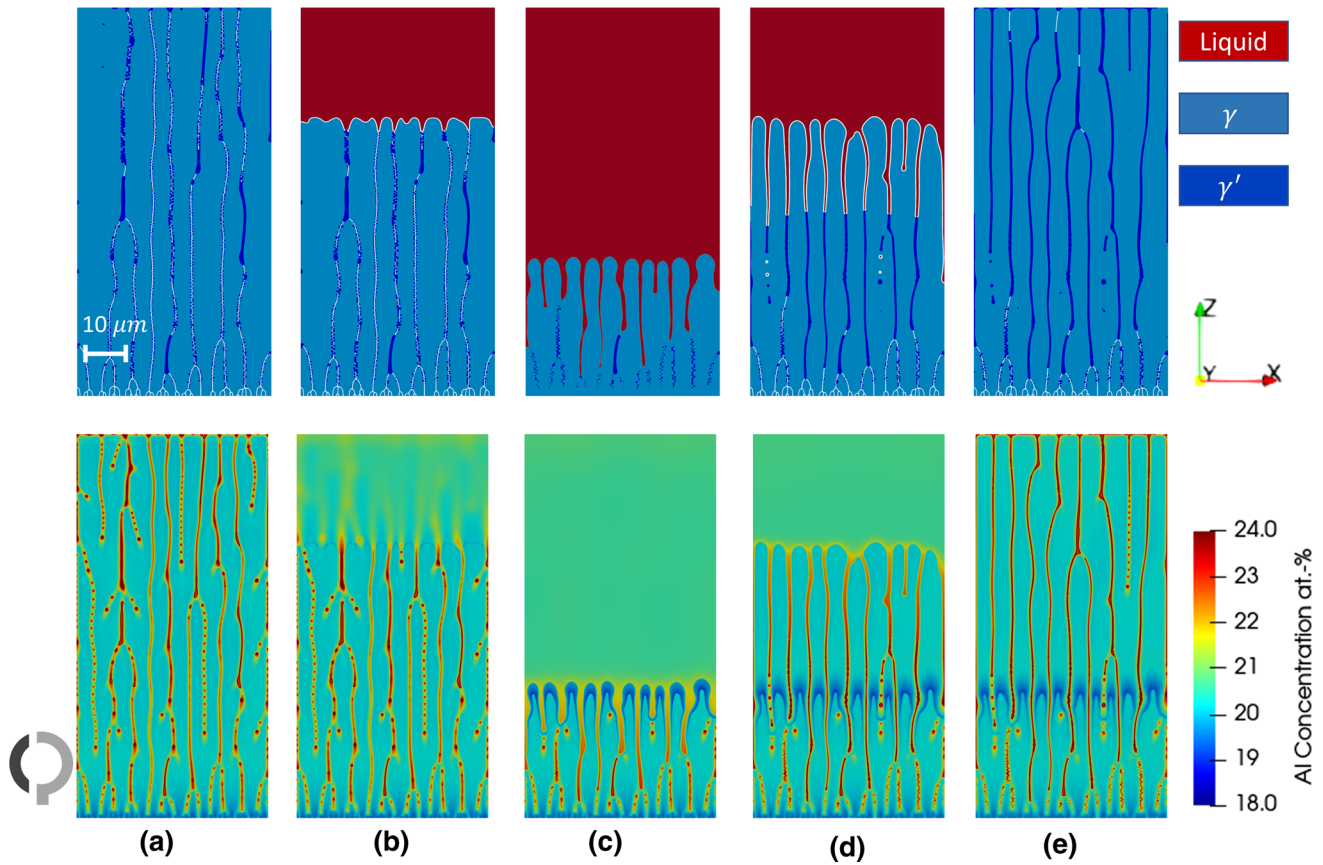


Fig. 8—Microstructure evolution and corresponding solute concentration during remelting and subsequent solidification of as-built sample: (a) previously built SX-like microstructure, (b) melting due to presence of heat source at the top, (c) end of melting and start of subsequent solidification, (d) later stage of solidification, (e) end of solidification.

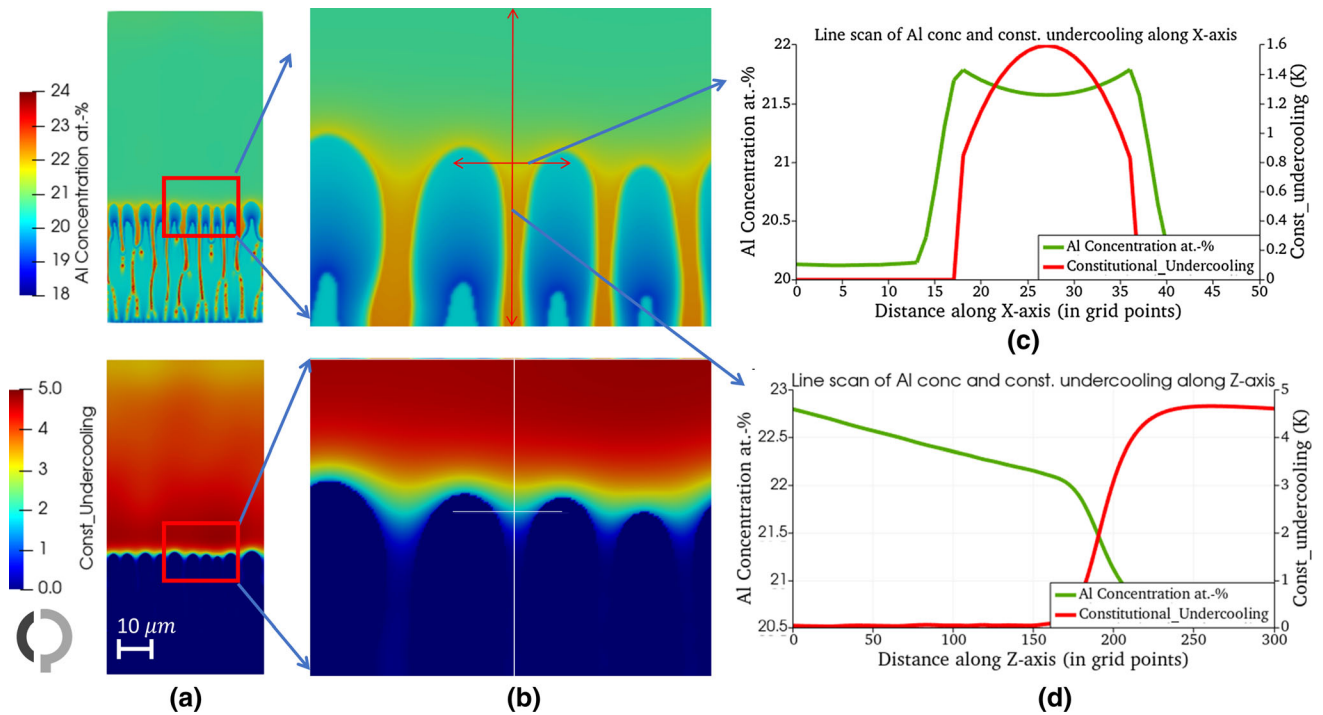


Fig. 9—(a) Spatial distribution of Al concentration and constitutional undercooling at the very beginning of solidification in remelted zone of as-built sample, (b) is the magnification of composition distribution and constitutional undercooling, (c, d) are the line scans of solute composition and constitutional undercooling over the sections of X-axis and Z-axis shown by the corresponding arrows.

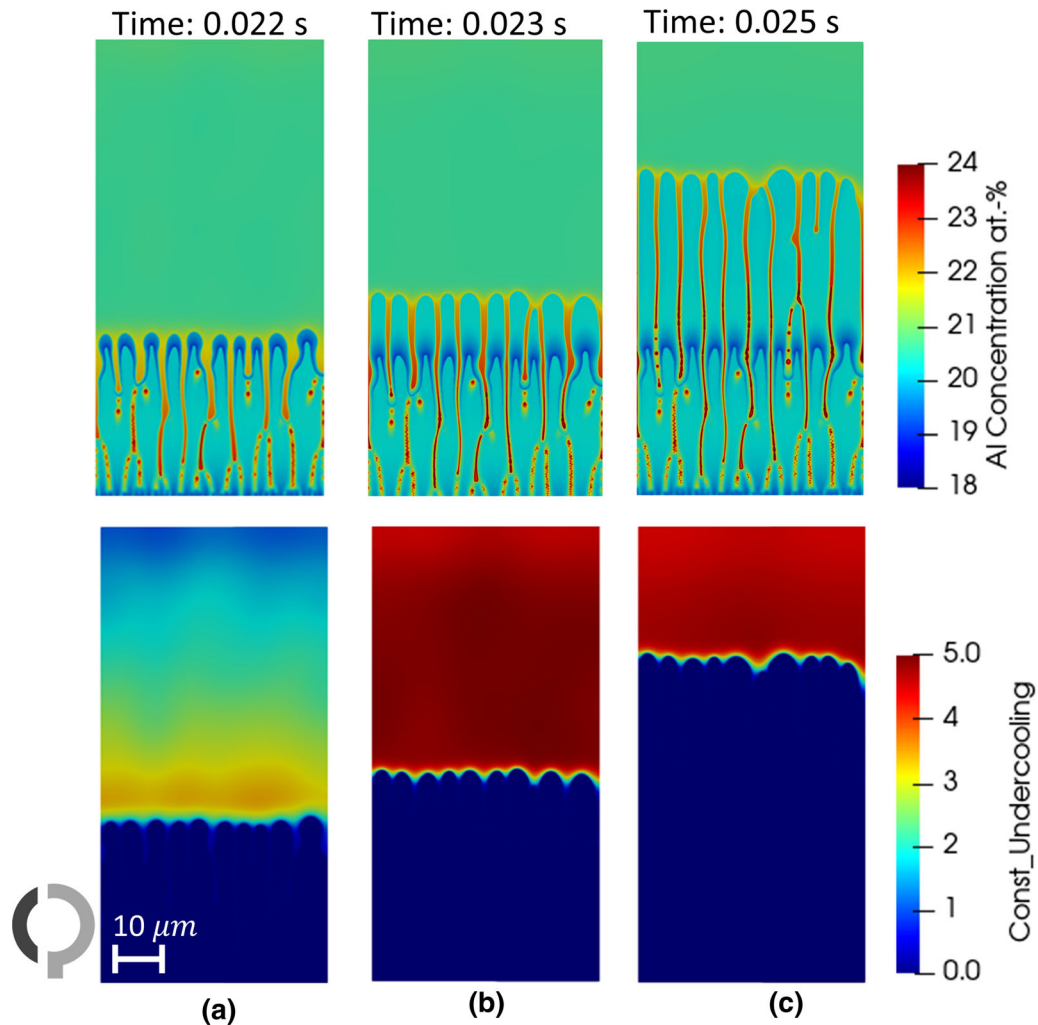
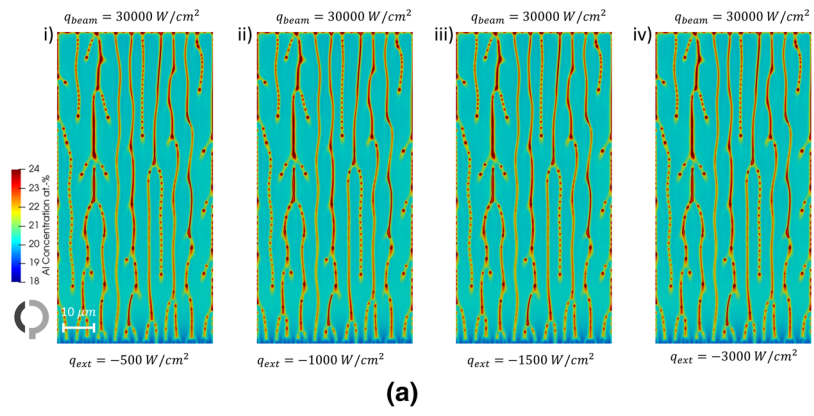


Fig. 10—Evolution of Al composition and corresponding constitutional undercooling during solidification in remelted zone of as-built sample at different simulated time: (a) 0.0022 s, (b) 0.0023 s and (c) 0.025 s.

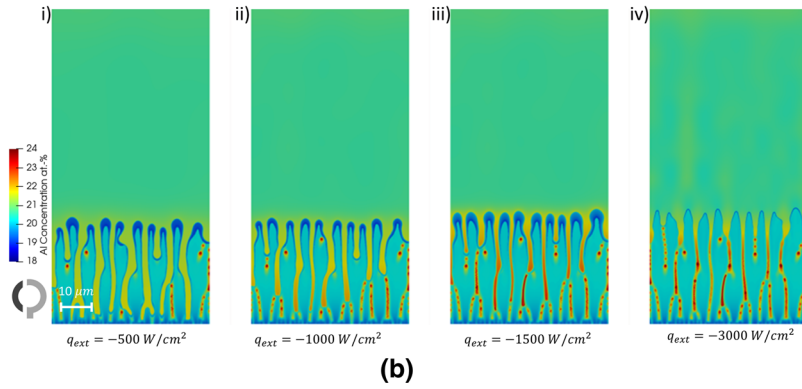
Figure 9 shows the simulation screenshot taken at the initial stage of solidification during remelting of the as-built sample. Figure 9(a) displays the solute composition and corresponding constitutional undercooling at the beginning of solidification, while Figure 9(b) highlights the local environment ahead of the solidification front. The solidification velocity at the onset of solidification calculated from Figure 9 is 7 mm s^{-1} which is significantly lower than the observed solidification velocity levels in rapid solidification. Figures 9(a) and (b) show that there is a significant concentration gradient in the interdendritic channels, resulting from deep melting of strongly segregated γ' phase. The distribution of Al concentration and constitutional undercooling across the interdendritic region and along the growth axis are shown by line scans presented in Figures 9(c), 9(d), respectively. The line scan along Z-axis shows that the constitutional undercooling gradually increases across the solidification front and that the maximum undercooling available at the start of solidification is about 4.6 K.

Figure 10 illustrates the evolution of Al concentration and calculated solute undercooling at three close time intervals during the start of solidification. Due to very low solidification velocities at the beginning of solidification, the initial solid grows with lower concentration of Al resulting in a small solute depletion layer. However, as seen in Figures 10(b) and (c), as dendrites start to grow, the solidification velocity increases rapidly, resulting in uniform solute composition in the dendrite trunks. The established composition gradient caused by remelting of the interdendritic channels leads to an increase in calculated constitutional undercooling over time. The maximum undercooling ahead of the solidification front, however, is limited to less than 5 K, as seen in Figure 10. Further, since the remelting simulations are performed under the same thermal boundary conditions as initial microstructure, there is no significant deviation in the dendrite arm spacing.

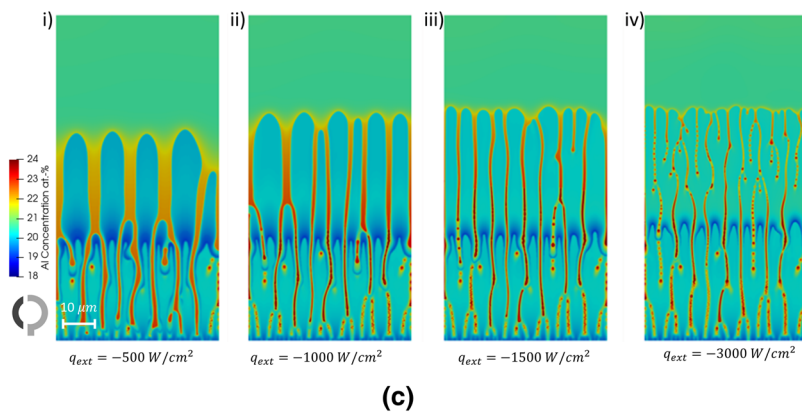
From the above analysis, we can conclude that in as-built sample, remelting creates significant composition gradient (refer to Al concentration plot in Figure 9) at interdendritic region. However, new grains can only



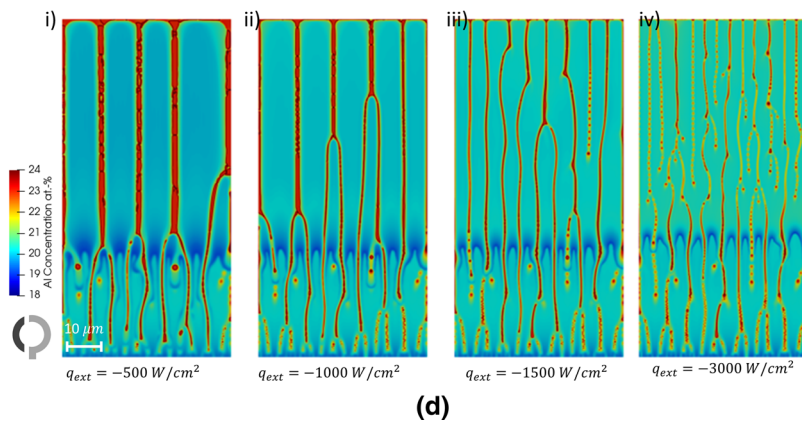
(a)



(b)



(c)



(d)

◀Fig. 11—Evolution of Al concentration during remelting and re-solidification under different heat extraction rates. (a) As-built microstructures are subjected same heating at the top and different heat extraction rates at the bottom. (b) Distribution of Al concentration at the end of remelting. (c) Distribution of Al concentration during the re-solidification. (d) Distribution of Al concentration towards the end of solidification.

form if the resulting constitutional undercooling is higher than the critical undercooling required for nucleation. Figure 10 also shows that the constitutional undercooling ahead of the solidification front increases gradually until it reaches a maximum, then it decreases continuously. This indicates that, under the process conditions of AM, it is unlikely to see nucleation of stray grains ahead of the solidification front, except for the melt pool border where the solidification velocities are much lower. Even if new grains nucleate, they can only survive if their growth axis is aligned with the direction of heat extraction. However, experiments have shown that it is still possible to get stray grains at the flank regions where the growth axis does not align with heat extraction direction.

1. Influence of solidification conditions on nucleation during remelting of as-built sample

The results presented in the previous section were obtained by performing remelting simulations under the same heat extraction rate as imposed during creation of as-built microstructure. However, as reported in References 14 and 15, nucleation observed at the melt pool border is significant when there is change of solidification conditions, such as enhanced cooling rate during remelting. To better understand the influence of solidification conditions on remelting of as-built sample, we have performed additional simulations with both reduced and enhanced heat extraction rates. In two simulations, the as-built sample is subjected to heat extraction rates of -500 W cm^{-2} and -1000 W cm^{-2} , which are lower than the as-built heat extraction rate (-1500 W cm^{-2}), and in one simulation, the sample is subjected to -3000 W cm^{-2} which is two times the as-built heat extraction rate.

Figures 11(a) through (d) present the evolution of dendritic microstructure along with Al concentration during various stages of remelting and re-solidification. Figure 11(a), (i) through (iv) show the as-built microstructure, which is obtained with a heat extraction rate of -1500 W cm^{-2} . The as-built microstructure is then subjected to remelting under four different heat extraction rates to study the influence of changes in heat extraction rates during remelting. Figure 11(b), (i) through (iv) present the state of microstructures at the end of remelting and the onset of re-solidification. It is clear from these figures that the depth of remelting in the interdendritic channels varies depending on the heat extraction rate. The interdendritic channels in the microstructure subjected to lower heat extraction rates are completely remelted, while those in the microstructure subjected to higher heat extraction rates remain

intact. Figure 11(c), (i) through (iv) shows that during re-solidification, the system always tries to adjust to the equilibrium dendrite spacing according to the applied heat extraction rate. Therefore, in microstructures subjected to lower heat extraction rates, the number of dendrites is reduced, resulting in increased interdendritic spacing. Whereas, in microstructure subjected to higher heat extraction rate tip splitting can be observed which reduces interdendritic spacing. Finally, Figures 11(d), (i) through (iv) show the fully re-solidified microstructures towards the end of solidification with the interdendritic channels transformed to eutectic γ' phase.

To further understand the local solidification conditions during remelting under different heat extraction rates, we have analysed the solute concentration distribution and constitutional undercooling at the onset of solidification. As shown in Figure 12, the segregation of Al in the interdendritic channels increases with increasing heat extraction rate. Additionally, the constitutional undercooling also increases with the heat extraction rate. In Figures 12(a) and (b), which correspond to the lower heat extraction rates, the undercooling is significantly lower compared to the undercooling observed in Figures 12(c) and (d), corresponding to the higher heat extraction rates. This suggests that the chances of nucleation during remelting are lower under the conditions imposed in Figures 12(a) and (b). A similar effect is observed in References 15 and 48, where higher undercooling during re-solidification resulted in dendrite tip splitting and promoted nucleation of stray grains.

C. Remelting of Homogenized Sample

In order to further understand the impact of solidification conditions on remelting, simulations of a homogenized SX sample were performed. The key objective of these simulations is to understand the local environment at the melt pool border at the start of solidification. Two methods are considered to obtain the homogenized microstructure. The first method involves heating and holding the as-built solidification microstructure until it is fully homogenized, similar to the process used experimentally for the CMSX-4 alloy in Reference 15. In this approach, the system is heated until all existing γ' phase is dissolved, and then held at a constant temperature until the composition of Al is completely homogenized. The second method involves starting the simulation with a complete solid state of the γ phase with the composition of Al as the nominal composition, assuming complete homogenization. Both methods are tested, but the presence of dendrite boundaries even after complete homogenization in the first method resulted in artificial triple junctions formation during remelting. Therefore, the simulations are continued with the microstructure obtained from the second method. To perform remelting simulations, the same procedure is followed as in the remelting of the as-built sample, activating the heat source at the start of the simulation and deactivating it when the volume fraction of liquid reaches 60 pct.

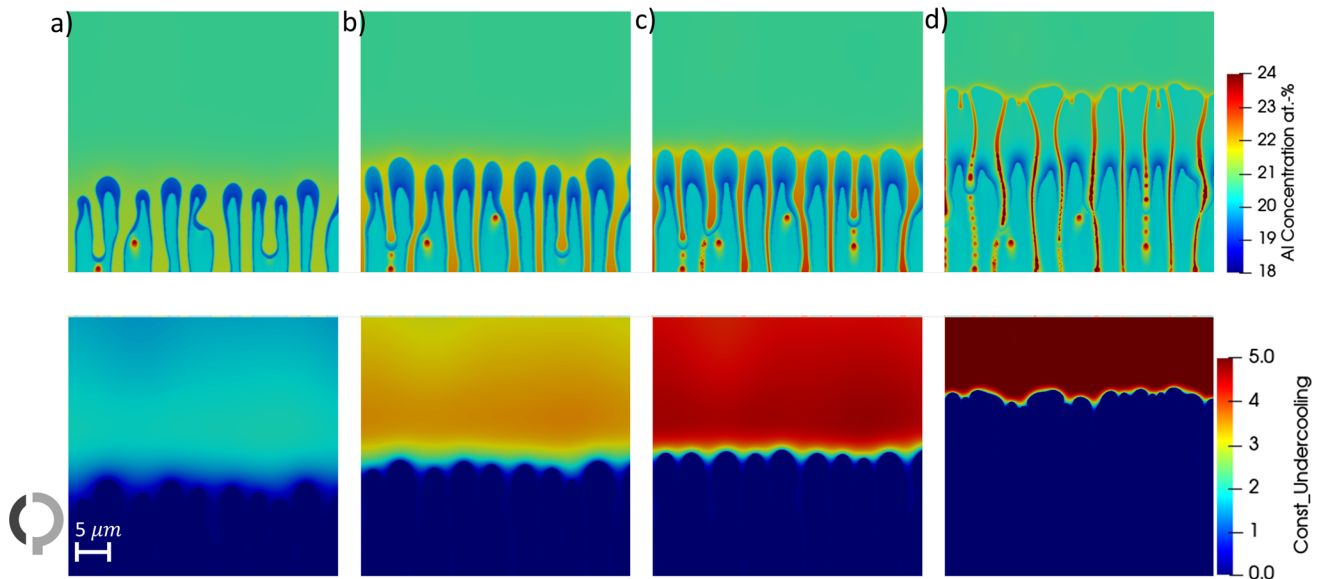


Fig. 12—Enhanced view of evolution of Al concentration and total undercooling at the start of solidification of as-built sample subjected to heat extraction rates of (a) – 500 W cm^{-2} , (b) – 1000 W cm^{-2} , (c) – 1500 W cm^{-2} , and (d) – 3000 W cm^{-2} .

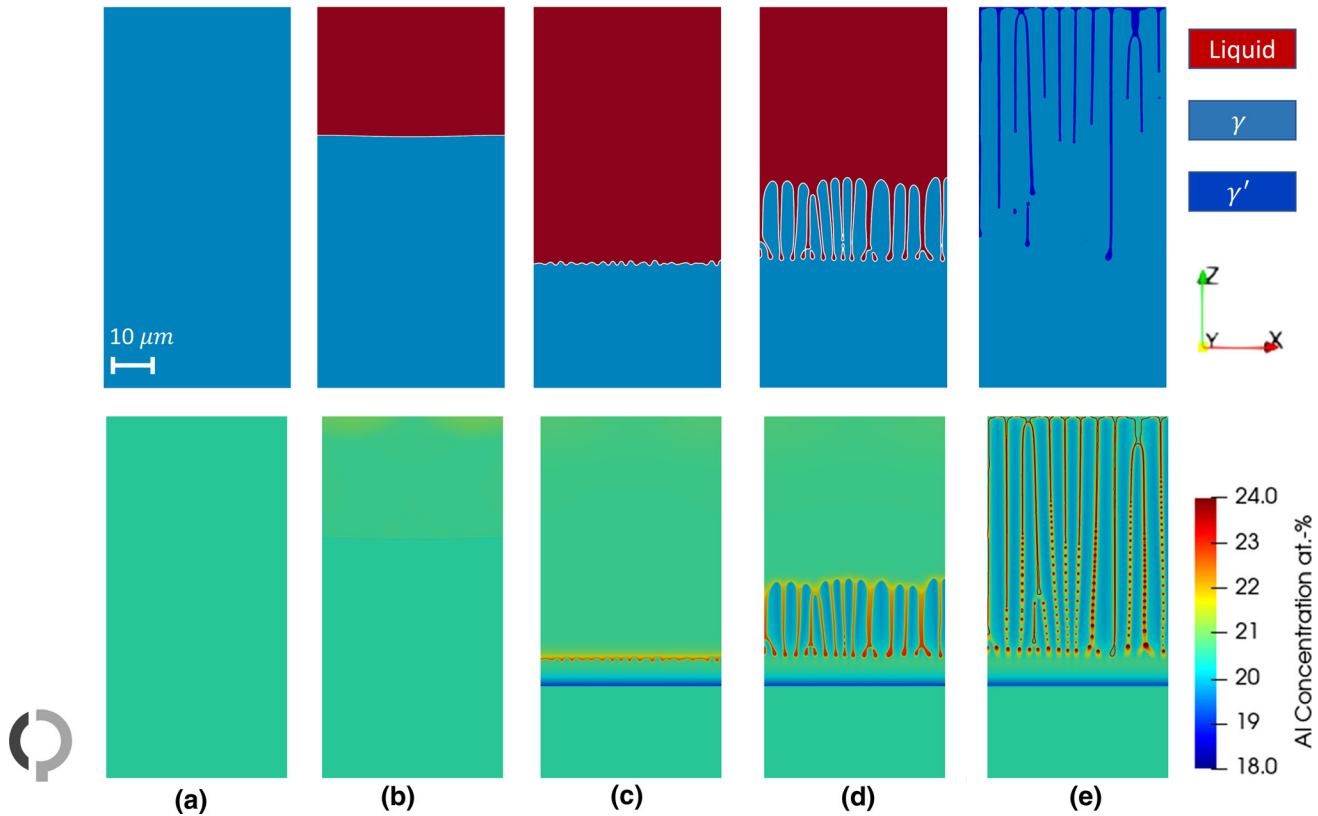


Fig. 13—Microstructure evolution and corresponding solute concentration during remelting and subsequent solidification of homogenized SX sample: (a) initial microstructure with complete homogenization, (b) melting due to presence of heat source at the top, (c) breakdown of planar front and start of subsequent solidification, (d) later stage of solidification, (e) end of solidification.

Figure 13 shows the microstructure evolution and the corresponding composition distribution of Al during remelting and solidification of homogenized SX sample.

The initial microstructure, obtained from a complete solid state with nominal Al composition, is shown in Figure 13(a). As opposed to the melt pool border seen in

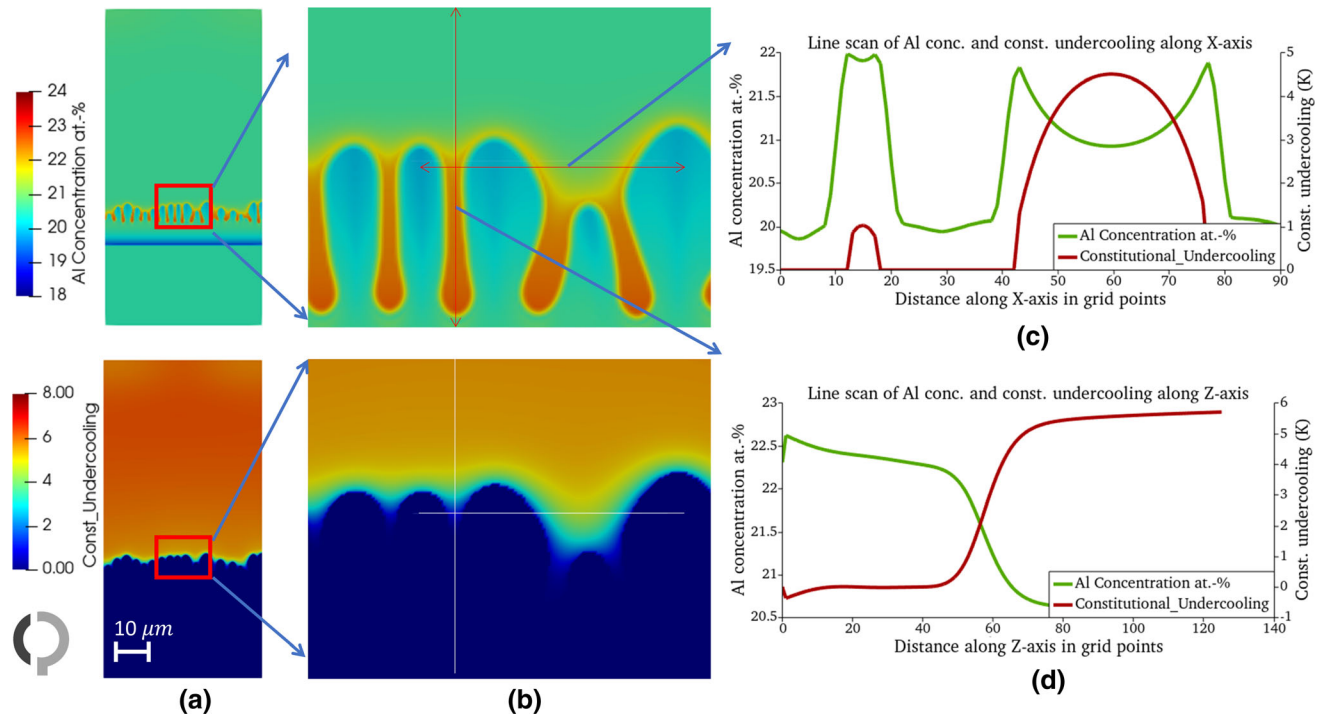


Fig. 14—(a) Spatial distribution of Al concentration and constitutional undercooling at the very beginning of solidification in remelted zone of homogenized SX sample, (b) magnification of distribution of composition and constitutional undercooling, (c) line scan of solute composition and constitutional undercooling over the section of X-axis shown by the arrow (d) line scan of solute composition and constitutional undercooling over the section of Z-axis shown by the arrow.

the remelting of the as-built sample (shown in Figure 8(b)), the melt pool border in the homogenized case (Figure 13(b)) is more uniform due to a single solid phase and a uniform solute composition. At the beginning of re-solidification (Figure 13(c)), the solidification front grows initially as planar due to the low solidification velocity and negligible concentration gradient. However, the melt pool boarder creates a layer with depleted composition at the solidification front, which results in subsequent composition gradient ahead of it similar to the experiment (Figure 1(b)). Due to the composition gradient and perturbations caused by the numerical modeling, the planar front disappears and cellular dendrites start to grow with significant segregation of Al into interdendritic regions, as shown in Figure 13(d). The end of solidification is shown in Figure 13(e), where γ' is nucleating and grows in the interdendritic regions of the remelted section.

Figures 14 and 15 present a more detailed view of local environment at the melt pool interface at the start of solidification of homogenized SX sample. From Figure 14 it is evident that in the homogenized SX sample, remelting is more uniform than in the as-built case due to the absence of grain boundaries. As shown in Figure 14(a), there exists a significant solute depletion resulting from zero solidification velocity at the onset of re-solidification due to change of direction of heat flux from positive to negative. The length of the planar front growth, *i.e.* the distance between the solute depletion layer and the dendritic solidification front, is found to be

5 μm which is in close agreement with experimental studies conducted on the SX sample of CMSX-4 material under homogenized conditions.^[15] Figure 14(c) presents the Al concentration and calculated constitutional undercooling along the line scan perpendicular to the growth axis. From this plots it is clear that even in remelting of homogenized sample, once the planar front breaks down, dendrite arms grow with solute segregation in the interdendritic liquid. As shown in the line scan drawn along the growth axis (Figure 14(c)), the undercooling in the homogenized case is comparatively higher than the undercooling obtained from the remelting of the as-built sample.

Figure 15 presents the evolution of Al concentration and corresponding constitutional undercooling during solidification in the remelted zone of homogenized SX sample. As shown in Figure 15(a), during the initial planar growth there is a uniform solute concentration ahead of the solidification front, which results in very high constitutional undercooling values. Next, Figures 15(b) and (c) show, that once the cellular dendrites start to grow, the composition gradient continues to rise in the interdendritic liquid region, but the resulting constitutional undercooling continues to decrease.

From the above results we can conclude that the simulation results are in close agreement with the experimental observation made in Reference 15, where nucleation is observed at some distance from the melt pool border during remelting of homogenized SX sample.

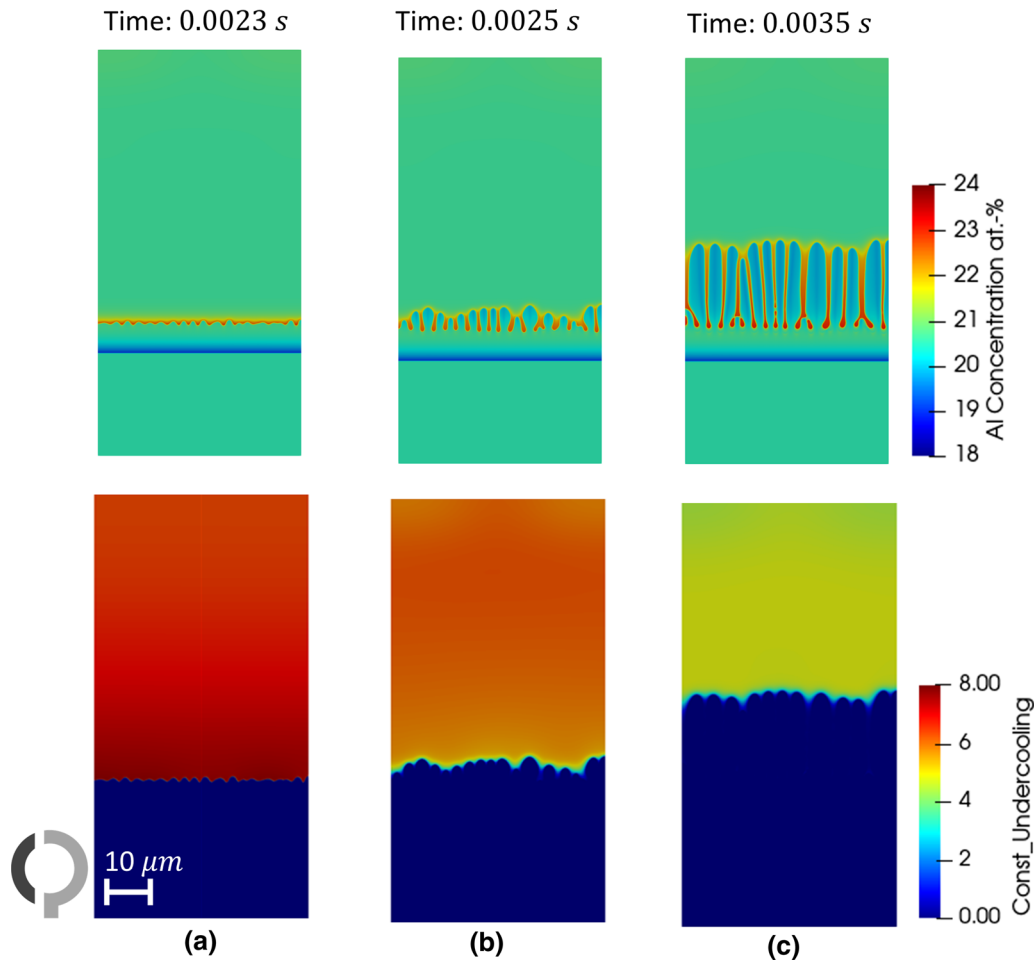


Fig. 15—Evolution of Al concentration and constitutional undercooling at the beginning of solidification in remelted zone of homogenized SX sample taken at different simulated time: (a) 0.0023 s, (b) 0.0025 s, (c) 0.0035 s.

V. SUMMARY AND CONCLUSIONS

To summarize, in the current work, the history-effect of partial remelting on nucleation is studied using the phase-field modeling. A coupled approach considering heat diffusion and phase-field evolution is used to simulate solidification and remelting in both as-built and homogenized states for a model binary system of Ni–20.5 mol pct Al. The numerical model is validated with experimental observations also conducted on the same binary alloy. From the obtained results the following conclusions can be drawn:

- Results obtained for the as-built solidification microstructure show that,
 - Al has a strong tendency to segregate in interdendritic liquid, promoting the formation of γ' phase.
 - The release of latent heat during solidification strongly influences the solidification velocity and cooling behavior, thereby affecting the solidification microstructure.
 - Cooling rate during solidification is found to be up to 10 times lower than the cooling rate at the

end of solidification which is generally measured as the cooling rate in the experiments.

- The simulation results obtained for the as-built remelting indicate that
 - Remelting is non-homogeneous due to the presence of strongly segregated γ' phase in the interdendritic regions.
 - Analysis of solidification velocity, Al concentration, and constitutional undercooling reveals the mechanisms responsible for nucleation of new grains at the melt pool border.
 - At the beginning of re-solidification, the solidification front moves with very low velocity and higher undercooling, which may lead to nucleation of new grains at the melt pool border. Nucleation of new grains is suppressed at the later stages of solidification as the cellular dendrites grow with higher solidification velocities, making classical CET impossible under AM process conditions.
- Further, simulation results obtained for remelting of as-built microstructure under reduced and enhanced heat extraction conditions demonstrate that

- Due to the variations in the effective cooling rate, the system tends to adjust to the equilibrium dendrite spacing.
- This results in increased dendrite spacing in simulations with lower heat extraction rate, and increased constitutional undercooling and dendrite tip splitting in simulations with higher heat extraction rate.
- In contrast to the microstructure evolution observed in as-built case, the simulation results for remelting of homogenized SX samples show, that
 - Remelting is more uniform due to the presence of a single solid phase and uniform solute composition throughout the system.
 - At the beginning of re-solidification the front grows in a planar manner with very low solidification velocity until it is disturbed by the increased solute concentration and constitutional undercooling in the interdendritic regions.
 - This creates the condition for nucleation of new grains at some distance from the melt pool border. These results are in close agreement with the experimental observation in Reference 15 where the nucleation is observed at some distance into the melt pool border during remelting of homogenized CMSX-4 sample.

Finally, we can conclude that the understanding gained from this investigation greatly helps in controlling nucleation of stray grains in SEBM of Ni-based superalloys. In the current study, we limited the phase-field simulations to a binary alloy and apply the quasi-equilibrium approach for solute redistribution.^[49] Future work will be concentrated on the effect of multi-component solidification and to include the effects of solute trapping applying the finite interface dissipation (FID) model for non-equilibrium transformation.^[50,51]

ACKNOWLEDGMENTS

We gratefully acknowledge the help of J. Renner and C. Breuning for the electron beam melting experiments. Further, we thank S. Michel for performing the EPMA measurements and N. Semjatov for the EBSD mappings.

AUTHOR CONTRIBUTIONS

Conceptualizations, M.U.; methodology, M.U. and I.S.; software, M.U. and O.S.; experiments, B.W. and C.K.; experimental characterization, B.W.; model validation, M.U. and I.S.; formal analysis, M.U. and I.S.; investigation, M.U. and I.S.; visualizations, M.U. and

B.W.; supervision, O.S., I.S., and C.K.; project administration, U.M. and I.S.; funding acquisition, I.S. and C.K.

FUNDING

Open Access funding enabled and organized by Projekt DEAL. The research was funded by the Deutsche Forschungsgemeinschaft (DFG) via projects C5 and B2 of the collaborative research center SFB/103 “From Atoms to Turbine Blades”.

COMPETING INTERESTS

The authors declare that they have no known competing financial interest or personal relationships that could have appeared to influence the work reported in this paper.

OPEN ACCESS

This article is licensed under a Creative Commons Attribution 4.0 International License, which permits use, sharing, adaptation, distribution and reproduction in any medium or format, as long as you give appropriate credit to the original author(s) and the source, provide a link to the Creative Commons licence, and indicate if changes were made. The images or other third party material in this article are included in the article’s Creative Commons licence, unless indicated otherwise in a credit line to the material. If material is not included in the article’s Creative Commons licence and your intended use is not permitted by statutory regulation or exceeds the permitted use, you will need to obtain permission directly from the copyright holder. To view a copy of this licence, visit <http://creativecommons.org/licenses/by/4.0/>.

REFERENCES

1. U.M. Dilberoglu, B. Gharehpapagh, U. Yaman, and M. Dolen: *Procedia Manuf.*, 2017, vol. 11, pp. 545–54.
2. M. Attaran: *Business Horizons*, 2017, vol. 60(5), pp. 677–88.
3. ASTM F2792-12a: *Standard Terminology for Additive Manufacturing Technologies*. Standard, ASTM International, 2015.
4. D. Herzog, V. Seyda, E. Wycisk, and C. Emmelmann: *Acta Mater.*, 2016, vol. 117, pp. 371–92.
5. N. Guo and M.C. Leu: *Front. Mech. Eng.*, 2013, vol. 8(3), pp. 215–43.
6. F. Calignano, D. Manfredi, E.P. Ambrosio, S. Biamino, M. Lombardi, E. Atzeni, A. Salmi, P. Minetola, L. Iuliano, and P. Fino: *Proc. IEEE*, 2017, vol. 105(4), pp. 593–612.
7. L. Ladani and M. Sadeghilaridjani: *Metals*, 2021, vol. 11(9), p. 1391.
8. Y. Li, X. Liang, Y. Yefeng, D. Wang, and F. Lin: *Chin. J. Mech. Eng. Addit. Manuf. Front.*, 2022, vol. 1, p. 100019.
9. T.M. Pollock, A.J. Clarke, and S.S. Babu: *Metall. Mater. Trans. A*, 2020, vol. 51A(12), pp. 6000–019.

10. H. Helmer, A. Bauereiß, R.F. Singer, and C. Körner: *Mater. Sci. Eng. A*, 2016, vol. 668, pp. 180–87.
11. X. Liu, C. Zhao, X. Zhou, Z. Shen, and W. Liu: *Mater. Des.*, 2019, vol. 168, p.107677.
12. P. Karimi, E. Sadeghi, J. Ålgårdh, and J. Andersson: *Mater. Charact.*, 2019, vol. 148, pp. 88–99.
13. X. Wang, P.W. Liu, Y. Ji, Y. Liu, M.H. Horstemeyer, and L. Chen: *J. Mater. Eng. Perform.*, 2019, vol. 28(2), pp. 657–65.
14. A.M. Rausch, M.R. Gotterbarm, J. Pistor, M. Markl, and C. Körner: *Materials*, 2020, vol. 13(23), p. 5517.
15. A.M. Rausch, J. Pistor, C. Breuning, M. Markl, and C. Körner: *Materials*, 2021, vol. 14(12), p. 3324.
16. K. Harris, G.L. Erickson, S.L. Sikkenga, W.D. Brentnall, J.M. Aurrecoechea, and K.G. Kubarych: *J. Mater. Eng. Perform.*, 1992, vol. 2(4), pp. 481–87.
17. T.M. Pollock and S. Tin: *J. Propul. Power*, 2006, vol. 22(2), pp. 361–74.
18. D.R. Gunasegaram and I. Steinbach: *Metals*, 2021, vol. 11(9), p. 1425.
19. A.R.A. Dezfoli, Y.-L. Lo, and M.M. Raza: *Crystals*, 2021, vol. 11(9), p. 1065.
20. M. Yang, L. Wang, and W. Yan: *Npj Comput. Mater.*, 2021, vol. 7(1), pp. 1–12.
21. I. Steinbach: *Acta Mater.*, 2008, vol. 56(18), pp. 4965–71.
22. M. Uddagiri, J. Spee, S. Hubig, and I. Steinbach: *IOP Conference Series: Materials Science and Engineering*, vol. 861, IOP Publishing, Bristol, 2020, p. 012014.
23. T. Keller, G. Lindwall, S. Ghosh, L. Ma, B.M. Lane, F. Zhang, U.R. Kattner, E.A. Lass, J.C. Heigel, Y. Idell, *et al.*: *Acta Mater.*, 2017, vol. 139, pp. 244–53.
24. T. Pinomaa and N. Provatas: *Acta Mater.*, 2019, vol. 168, pp. 167–77.
25. M. Conti: *Phys. Rev. E*, 1998, vol. 58(5), p. 6166.
26. B. Böttger and M. Apel: *Procedia CIRP*, 2022, vol. 111, pp. 291–95.
27. T. Wang, D. Wexler, L. Guo, Y. Wang, and H. Li: *Materials*, 2022, vol. 15(16), p. 5517.
28. K. Karayagiz, L. Johnson, R. Seede, V. Attari, B. Zhang, X. Huang, S. Ghosh, T. Duong, I. Karaman, A. Elwany, *et al.*: *Acta Mater.*, 2020, vol. 185, pp. 320–39.
29. C. Tang and H. Du: *JOM*, 2022, pp. 1–14.
30. H. Schaar, I. Steinbach, and M. Tegeler: *Metals*, 2021, vol. 11(12), p. 2012.
31. C. Arnold, C. Pobel, F. Osmanlic, and C. Körner: *Rapid Prototyping J.*, 2018, vol. 24(8), pp. 1401–06.
32. M. Ramsperger, R.F. Singer, and C. Körner: *Metall. Mater. Trans. A*, 2016, 47A(3), pp. 1469–80.
33. I. Steinbach, F. Pezzolla, B. Nestler, M. Seeßelberg, R. Prieler, G.J. Schmitz, and J.L.L. Rezende: *Physica D Nonlinear Phenom.*, 1996, vol. 94(3), pp. 135–47.
34. I. Steinbach, B. Böttger, J. Eiken, N. Warnken, and S.G. Fries: *J. Phase Equilib. Diffus.*, 2007, vol. 28(1), pp. 101–106.
35. I. Steinbach: *Model. Simul. Mater. Sci. Eng.*, 2009, vol. 17(7), p. 073001.
36. A. Karma: *Phys. Rev. Lett.*, 2001, vol. 87(11), p. 115701.
37. S.G. Kim: *Acta Mater.*, 2007, vol. 55(13), pp. 4391–99.
38. B. Echebarria, R. Folch, A. Karma, and M. Plapp: *Phys. Rev. E*, 2004, vol. 70(6), p. 061604.
39. J. Goldak, A. Chakravarti, and M. Bibby: *Metall. Trans. B*, 1984, vol. 15(2), 299–305 (1984).
40. OpenPhase Academic: <https://openphase.rub.de/>. Accessed 04 August 2022.
41. M. Tegeler, O. Shchyglo, R.D. Kamachali, A. Monas, I. Steinbach, and G. Sutmann: *Comput. Phys. Commun.*, 2017, vol. 215, pp. 173–87.
42. Thermo-Calc Software TTNI7 Nickel based-alloys database. <https://thermocalc.com/products/databases/nickel-based-alloys/>. Accessed 04 August 2022.
43. A.L. Greer, A.M. Bunn, A. Tronche, P.V. Evans, and D.J. Bristow: *Acta Mater.*, 2000, vol. 48(11), pp. 2823–35.
44. A. Monas, O. Shchyglo, D. Höche, M. Tegeler, and I. Steinbach: *IOP Conference Series: Materials Science and Engineering*, vol. 84, IOP Publishing, Bristol, 2015, p. 012069.
45. J. Kundin, L. Mushongera, and H. Emmerich: *Acta Mater.*, 2015, vol. 95, pp. 343–56.
46. J.A. Koepf, D. Soldner, M. Ramsperger, J. Mergheim, M. Markl, and C. Körner: *Comput. Mater. Sci.*, 2019, vol. 162, pp. 148–55.
47. W. Kurz, B. Giovanola, and R. Trivedi: *Acta Metall.*, 1986, vol. 34(5), pp. 823–30.
48. H. Helmer, A. Bauereiß, R.F. Singer, and C. Körner: *Mater. Sci. Eng. A*, 2016, vol. 668, pp. 180–87.
49. J. Eiken, B. Böttger, and I. Steinbach: *Phys. Rev. E*, 2006, vol. 73, p. 066122.
50. I. Steinbach, L. Zhang, and M. Plapp: *Acta Mater.*, 2012, vol. 60(6–7), pp. 2449–3246.
51. L. Zhang and I. Steinbach: *Acta Mater.*, 2012, vol. 60, pp. 2702–710.

Publisher’s Note Springer Nature remains neutral with regard to jurisdictional claims in published maps and institutional affiliations.